ACS APPLIED MATERIALS & INTERFACES

Research Article

www.acsami.org

First-Principles Investigations of the Working Mechanism of 2D *h*-BN as an Interfacial Layer for the Anode of Lithium Metal Batteries

Le Shi, Ao Xu, and Tianshou Zhao*

Department of Mechanical and Aerospace Engineering, The Hong Kong University of Science and Technology, Clear Water Bay, Kowloon, Hong Kong, China

ABSTRACT: An issue with the use of metallic lithium as an anode material for lithium-based batteries is dendrite growth, causing a periodic breaking and repair of the solid electrolyte interphase (SEI) layer. Adding 2D atomic crystals, such as *h*-BN, as an interfacial layer between the lithium metal anode and liquid electrolyte has been demonstrated to be effective to mitigate dendrite growth, thereby enhancing the Columbic efficiency of lithium metal batteries. But the underlying mechanism leading to the reduced dendrite growth remains unknown. In this work, with the aid of first-principle calculations, we find that the interaction between the *h*-BN and lithium metal layers is a weak van der Waals force, and two atomic layers of *h*-BN are thick enough to block the electron tunneling from lithium metal to electrolyte, thus prohibiting the decomposition of electrolyte. The interlayer spacing between the *h*-BN and lithium metal layers can provide larger adsorption energies toward lithium atoms than that provided by bare lithium or *h*-BN, making lithium atoms prefer to intercalate under the cover of *h*-BN during the plating process. The combined high stiffness of *h*-BN and the low diffusion energy barriers of lithium at the Li/*h*-BN interfaces induce a uniform distribution of lithium under *h*-BN, therefore effectively suppressing dendrite growth.

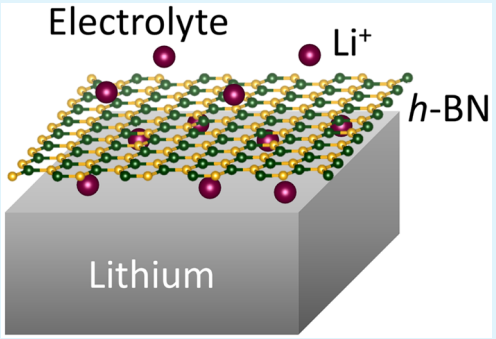

KEYWORDS: *lithium metal anode, dendrite, Columbic efficiency, interfacial layer, h-BN, first-principles calculation*

1. INTRODUCTION

Under the ever-increasing demand for electrical energy storage devices with larger capacity and higher energy density, conventional lithium-ion batteries based on graphite anode can no longer provide satisfactory performance.[1−4] Tremendous efforts have been devoted to the development of next-generation anode materials.[5−7] Among all the possible choices, lithium metal anode has long been regarded as the "Holy Grail" for its highest energy density (3860 mAh/g) and lowest electrochemical potential (−3.04 V vs the standard hydrogen electrode),[8,9] and both lithium−sulfur batteries[10,11] and lithium−air batteries[12,13] are based on lithium metal anode. However, lithium metal anode suffers from the long-standing dendrite problem, which is rooted in the intrinsic properties of lithium metal and may cause short-circuit of the battery system. Lithium metal is very reactive and can spontaneously react with the organic electrolyte to form a passivation solid electrolyte interphase (SEI) layer. The formation of dendritic lithium will also cause periodic breaking and repair of the SEI layer, consuming a large amount of lithium and electrolyte and further leading to low Columbic efficiency and poor cycling stability of lithium metal batteries.[14−17]

Many strategies have been proposed to alleviate the dendrite problem, such as building lithium deposition scaffold to host the lithium metal,[18−20] adding additives to interfere the lithium deposition process,[21−24] changing the charging mode to mitigate the lithium ion accumulation,[25,26] and engineering the separator properties to realize homogeneous ion distribution[27,28] and so forth. All these methods could mitigate the dendrite growth phenomenon to some extent. However, as the mechanical strength provided by the naturally formed SEI is limited, the periodic breaking and repair of SEI layer which is responsible for the low Columbic efficiency still exist. To address this issue, an artificial SEI layer with better mechanical strength and good chemical stability, such as Al_2O_3[29] and Li_3PO_4,[30] have been proposed. While provided better mechanical properties, these rigid artificial SEI layers commonly suffer from low lithium ion conductivity and high interfacial impedance, which on the other hand limited the rate capability of the lithium metal anode.[31−35] New interfacial layer with strong mechanical strength, good chemical stability, high lithium ion conductivity and satisfying electron barrier property is urgently needed.

Yang et al. proposed a new concept of employing 2D atomic crystals as the interfacial layer in place of the 3D bulk material for lithium metal anode to suppress the dendrite growth, and *h*-BN has been chosen to demonstrate this concept for its high Young's modulus (∼1 TPa), excellent chemical stability and superior insulating property.[36] Several atomic layers of *h*-BN were deposited on the copper current collector to separate the lithium metal and liquid electrolyte, while the atomic defects on *h*-BN formed during the synthesis procedure were expected to

Received: November 14, 2016
Accepted: December 22, 2016
Published: December 22, 2016

DOI: 10.1021/acsami.6b14560
ACS Appl. Mater. Interfaces 2017, 9, 1987−1994

serve as lithium ion conduction pathways. By adding 2D *h*-BN as interfacial layer for lithium metal anode, the dendrite growth phenomenon was significantly inhibited, and the high Columbic efficiency was well preserved during the cycling test. In addition, according to the experiments, the atomic defects generated during the synthesis procedure can provide adequate ionic diffusion to maintain high Li^+ ions flux. However, as a new kind of interfacial layer, the detailed interaction between the 2D atomic crystals and lithium metal is still unknown, and how the 2D atomic crystals work to suppress the dendrite growth during the lithium plating process is yet to be explored. In this work, we systematically investigated the interaction between the 2D *h*-BN and lithium metal and explained how the *h*-BN suppress the lithium dendrite growth and maintain the high Columbic efficiency of lithium metal anode via first-principle calculations. From the interfacial models, we found that the interaction between *h*-BN and lithium metal is a weak van der Waals force, and two atomic layers of *h*-BN can provide energy barriers larger than 1.33 eV to block the electron tunneling from lithium to electrolyte, which protected the electrolyte from decomposition. The binding of lithium atoms at the Li/*h*-BN interfaces are stronger than those on bare lithium metal or *h*-BN surface. Thus, during the plating process, lithium atoms will prefer to intercalate under the cover of *h*-BN instead of exposing to the electrolyte, which prevented the lithium metal anode from corrosion. The high stiffness of *h*-BN and the low lithium diffusion energy barriers (<0.21 eV) at the Li/*h*-BN interfaces can work together to facilitate a uniform distribution of lithium at the Li/*h*-BN interfaces, further result in a flat lithium metal surface. Our research successfully explained how 2D *h*-BN acts as an interfacial layer for lithium metal anode to suppress the lithium dendrite growth and maintain the high Columbic efficiency, which will shed light on future design of lithium metal anode.

2. COMPUTATIONAL METHODOLOGY

All the computations were conducted using the Quantum ESPRESSO software package.[37] Perdew–Burke–Ernzerhof (PBE) generalized gradient approximation (GGA)[38] and projector augmented wave (PAW)[39] pseudopotentials were employed to treat the exchange-correlation functionals and electron–ion interactions. To describe the van der Waals interaction, Grimme's D2 correction was adopted.[40] The cutoff energy was set to be 78 Ry for all calculations. For geometrical optimization, the k-point mesh was set to be less than 0.05 $Å^{-1}$ and the force tolerance was set to be 0.01 eV $Å^{-1}$. For density of states (DOS) calculation, denser k-point mesh less than 0.01 $Å^{-1}$ was adopted.

Slab models were employed to calculate the surface energies and adsorption energies with 10–15 Å thick vacuum layers added to prevent the interaction between slabs. Five to seven layers of lithium atoms were considered when calculating the lithium metal surface energies to ensure convergence. The surface energies were calculated as follows:[16]

$$\gamma = \frac{1}{2A}(E^N_{\text{slab}} - N\mu_{\text{Li}}) \tag{1}$$

where A is the surface area, E^N_{slab} is the energy of the slab model containing N lithium atoms, and μ_{Li} is the chemical potential of metallic lithium. Lithium adsorption energy on lithium metal surfaces or *h*-BN or the Li/*h*-BN interfaces was calculated as follows:[41]

$$E_{\text{ads}} = E_{\text{tot}}(S/I + \text{Li}) - E_{\text{tot}}(S/I) - E_{\text{tot}}(\text{Li}) \tag{2}$$

where $E_{\text{tot}}(S/I + \text{Li})$ means the total energy of surface/interface adsorbed with lithium atom, $E_{\text{tot}}(S/I)$ means the total energy of the surface/interface and $E_{\text{tot}}(\text{Li})$ means the total energy of a single lithium atom. The interface formation energy of *h*-BN and lithium metal was calculated as follows:

$$E_{\text{f}} = \frac{E_{\text{Li}/h\text{-BN}} - E_{\text{Li-slab}} - E_{h\text{-BN}}}{A} \tag{3}$$

where A represents the surface area, $E_{\text{Li}/h\text{-BN}}$ represents the total energy of fully relaxed Li/*h*-BN interface model, $E_{\text{Li-slab}}$ represents the total energy of fully relaxed lithium surface slab model and $E_{h\text{-BN}}$ represents the total energy of fully relaxed *h*-BN. As the constructed Li/*h*-BN interface models are not coherent, another parameter namely interfacial energy σ was defined to evaluate the interaction between the two surfaces excluding the strain energy contribution, which can be calculated as follows:

$$\sigma = \frac{E_{\text{Li}/h\text{-BN}} - E_{\text{Li-slab}(z)} - E_{h\text{-BN}(z)}}{A} \tag{4}$$

where A is the surface area, $E_{\text{Li}/h\text{-BN}}$ is the total energy of the fully relaxed Li/*h*-BN interface model, and $E_{\text{Li-slab}(z)}$ and $E_{h\text{-BN}(z)}$ are the total energies of lithium slab model and *h*-BN with the same lattice parameters as the interface model along both the x and y directions and fully relaxed along the z direction. As the interaction between different atomic layers of *h*-BN is known to be weak van der Waals force, in the calculations of interfacial interactions between lithium metal and *h*-BN and lithium adsorption and diffusion at the Li/*h*-BN interfaces, only one atomic layer of *h*-BN was considered to save the computational efforts. In the density of states (DOS) calculation, two atomic layers of *h*-BN were considered to study the influence of lithium metal toward the electron tunneling energy barriers of *h*-BN. Nudged elastic band (NEB)[42] method was employed to calculate the lithium diffusion energy barriers, where 9, 9, and 32 images were used in the calculations of lithium diffusion on lithium metal surfaces, *h*-BN surface, and the Li/*h*-BN interfaces, respectively.

3. RESULTS AND DISCUSSION

3.1. Wulff Construction and Self-Adsorption and Diffusion of Lithium Metal. The optimized lattice parameter of lithium metal (*b.c.c*) was calculated to be 3.26 Å, which is in good agreement with experiments.[43] Three low-index surfaces, {001}, {110}, and {111} were chosen to study the surface energies, and the obtained energy values and the corresponding Wulff construction are shown in Figure 1. The general trend of

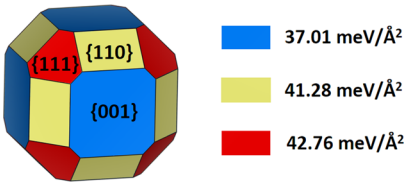

Figure 1. Wulff construction of lithium metal (*b.c.c*).

the calculated surface energies is in good agreement with previous calculations,[16,44] where the {001} surface shows the lowest surface energy while the {111} surface shows the highest. The little difference on detailed values may be caused by the consideration of van der Waals corrections. From the Wulff construction as shown in Figure 1, {001} and {110} surfaces occupy most of the exposed surface area of lithium metal. Thus, in the following sections, only these two surfaces were considered.

We then studied the lithium self-adsorption and diffusion on Li{001} and Li{110} surfaces. Three adsorption sites, hollow (H), bridge (B), and top (T) were considered as shown in Figure 2a. From the calculation results, for the Li{001} surface, H site shows the largest adsorption energy of −1.68 eV, while

DOI: 10.1021/acsami.6b14560
ACS Appl. Mater. Interfaces 2017, 9, 1987–1994

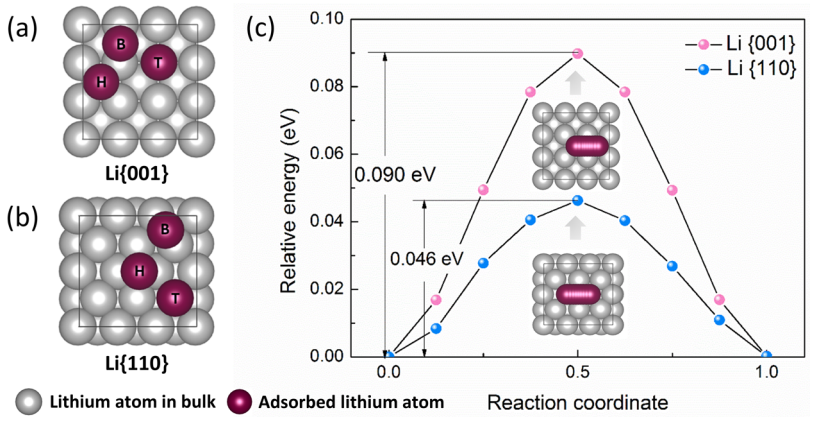

Figure 2. (a),(b) Lithium self-adsorption and (c) diffusion on Li{001} and Li{110} surfaces.

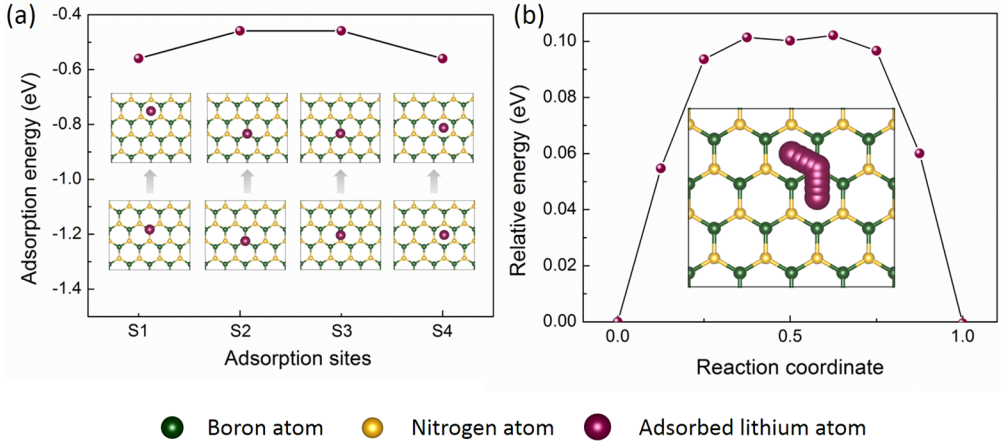

Figure 3. (a) Lithium adsorption and (b) diffusion on *h*-BN.

Table 1. Lattice Parameters of Li{001}, Li{110} and *h*-BN Supercells and the Constructed Interfaces after Geometrical Optimization

	$Li\{001\}_{3\times4}$	$h\text{-}BN_{4\times3}$	Li{001}/*h*-BN	$Li\{110\}_{3\times2}$	$h\text{-}BN_{4\times2}$	Li{110}/*h*-BN
a (Å)	9.78	10.04	10.00	9.78	10.04	10.08
b (Å)	13.04	13.05	13.03	9.22	8.70	8.75

Table 2. Structural Information and the Calculated Interface Formation Energy and Interfacial Energy of the Li/*h*-BN Interfaces

interface	matching	atom	misfit-*x* (%)	misfit-*y* (%)	E_f (meV/Å^2)	σ (meV/Å^2)
Li{001}/*h*-BN	3 × 4/4 × 3	108	2.57	0.059	−4.17	−5.85
Li{110}/*h*-BN	3 × 2/4 × 2	92	2.62	5.66	−1.49	−6.40

for the Li{110} surface, T site shows the largest adsorption energy of −1.85 eV. The diffusion energy barriers of lithium atom on these two surfaces were calculated as shown in Figure 2b. In both cases, the adsorbed lithium atom tends to directly reach to the other most stable adsorption site with an energy barrier of 0.090 and 0.046 eV respectively.

3.2. Lithium Adsorption and Diffusion on *h*-BN Monolayer. The optimized structure of *h*-BN shows a hexagonal lattice with a B—N bond length of 1.45 Å, which is in good agreement with experiments.[45] Four adsorption sites (above the N atom, above the B atom, bridge site and hollow site) were chosen to study the lithium adsorption behavior on *h*-BN as shown in Figure 3a. After geometrical optimization, lithium atom will move to either the hollow site or the top of N atom, with an adsorption energy of −0.56 eV and −0.46 eV, respectively. It can be found that the adsorption of lithium on *h*-BN is much weaker than those on lithium metal surfaces, thus during the lithium plating process, the lithium atom will not be deposited on the *h*-BN. The migration of lithium on *h*-BN is as shown in Figure 3b, where lithium will first migrate from the stable hollow site to the nearest N atom, and then migrate to the other nearest hollow site. The migration energy barrier of lithium on *h*-BN is calculated to be 0.10 eV.

3.3. Interfaces of Lithium Metal and *h*-BN. Two interfaces Li{001}/*h*-BN and Li{110}/*h*-BN were built to study the interaction between *h*-BN and lithium metal. A 3 × 4 supercell of Li{001} surface and a 4 × 3 supercell of *h*-BN were used to construct the Li{001}/*h*-BN interface, and a 3 × 2 supercell of Li{110} surface and a 4 × 2 supercell of *h*-BN were used to construct the Li{110}/*h*-BN interface. The lattice parameters for the considered supercells and interfaces after geometrical optimization are listed in Table 1. The lattice

DOI: 10.1021/acsami.6b14560
ACS Appl. Mater. Interfaces 2017, 9, 1987−1994

mismatches for the interfaces along both x and y directions are below 6% as shown in Table 2. It can be found that after geometrical optimization, the lattice parameters of h-BN are almost unchanged, while the lithium metal surfaces fit themselves to the lattice of h-BN, which is in accordance with the higher Young's modulus of h-BN.

After geometrical optimization, the structure of the considered two interfaces are shown in Figure 4. It can be found that for both cases, the interlayer spacing between h-BN and lithium metal surfaces are larger than 4.0 Å, which are large enough to accommodate another layer of lithium atoms intercalated. The calculated interface formation energy E_f and interfacial energy σ for the two interfaces are listed in Table 2, all of which are negative, indicating that the formation of such interfaces are thermodynamically preferable. The interactions between h-BN and lithium metal are quite weak, falling into the range of typical van der Waals interactions. For the Li{110}/h-BN interface, the large difference between E_f and σ is caused by the large strain energy originated from the structural deformation of the Li{110} surface to fit the lattice parameters of h-BN.

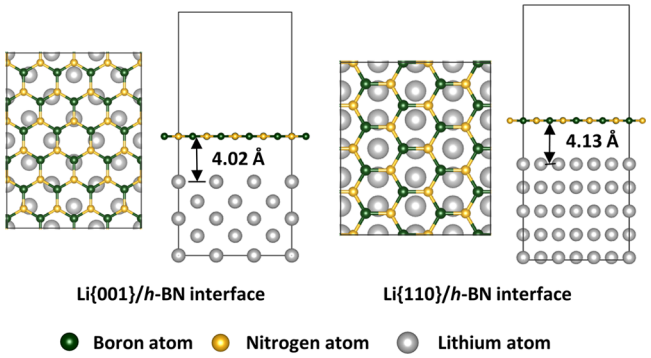

Figure 4. Geometries of Li{001}/h-BN interfaces.

We then investigated the electronic structure of the Li/h-BN interfaces. Two atomic layers of h-BN were taken into consideration to study the influence of lithium metal toward the density of states (DOS) of h-BN. The optimized geometry of Li{001}/2h-BN and Li{110}/2h-BN are shown in the inset of Figure 5. The distances between the two atomic layers of h-BN are 3.16 and 3.11 Å for the Li{001}/2h-BN and Li{110}/2h-BN cases respectively, which are similar to that in bulk h-BN. The distances between the first atomic layer of h-BN and lithium metal surfaces are close to the single atomic layer covered cases. From the DOS map, for both two interfaces, the covered two h-BN atomic layers exhibit an insulating property. However, for the first atomic layer of covered h-BN, small fluctuations on the right side of Fermi level can be observed which is induced by the interaction with lithium metal, while for the second atomic layer, the small fluctuations disappeared, and a wide bandgap of 4.3 eV close to that of the pristine h-BN was observed. According to Liu et al.,[16] the electron tunneling energy barrier from lithium metal across the covered interfacial layer can be estimated by the difference between the bottom of the conduction band and the Fermi level. Thus, for Li{001}/2h-BN, the electron tunneling energy barrier is about 1.33 eV, and for Li{110}/2h-BN, the electron tunneling energy barrier is about 1.65 eV. In both cases, the covered two atomic layers of h-BN can effectively block the electrons from transport to the electrolyte. This good insulating property ensures that lithium ions will plating under the cover of h-BN layers instead of above the h-BN, and also prevent the decomposition of electrolyte.

3.4. Lithium Adsorption between the Interfaces of Lithium Metal and h-BN. Eight symmetrically different adsorption sites were chosen to study the lithium adsorption at the interfaces of Li/h-BN as shown in Figure 6. It can be found that after geometrical optimization, the adsorbed lithium atom tends to migrate to the nearest hollow site or the N site under

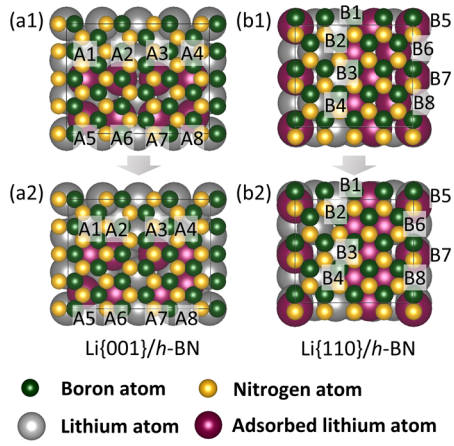

Figure 6. Adsorption sites of lithium atom at the Li/h-BN interfaces (a1),(b1) before and (a2),(b2) after geometrical optimization.

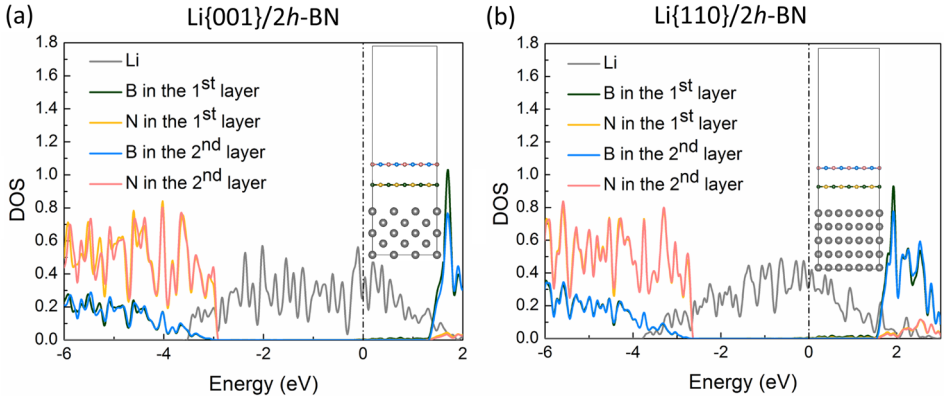

Figure 5. DOS of (a) Li{001}/h-BN and (b) Li{110}/h-BN interfaces with two atomic layers of h-BN covered.

DOI: 10.1021/acsami.6b14560
ACS Appl. Mater. Interfaces 2017, 9, 1987−1994

Table 3. Adsorption Energies of Lithium Atom at Different Adsorption Sites of the Interfaces and the Corresponding Height Variance of the Atoms in *h*-BN

Li{001}/*h*-BN Interface								
site	A1	A2	A3	A4	A5	A6	A7	A8
E_{ads} (eV)	−2.18	−2.04	−2.10	−2.17	−2.11	−2.12	−2.16	−2.13
$\overline{\Delta h_{BN}}$ (Å)	0.027	0.056	0.033	0.039	0.034	0.038	0.036	0.072
Li{110}/*h*-BN Interface								
site	B1	B2	B3	B4	B5	B6	B7	B8
E_{ads} (eV)	−2.29	−2.29	−2.29	−2.29	−2.21	−2.28	−2.19	−2.28
$\overline{\Delta h_{BN}}$ (Å)	0.018	0.017	0.018	0.017	0.014	0.018	0.016	0.018

the *h*-BN, which is similar to that on pristine *h*-BN. The calculated adsorption energies are listed in Table 3. For both of the two considered interfaces, the adsorption energies of lithium at the interfaces are much larger than those on pristine lithium surfaces or *h*-BN, indicating that compared with bare lithium metal or *h*-BN, lithium atoms will prefer to intercalate under the cover of *h*-BN. The larger adsorption energies ensure that during the lithium plating process, lithium will keep being deposited at the interlayer spacing between *h*-BN and lithium metal. For Li{001}/*h*-BN, the differences of adsorption energies among different adsorption sites are smaller than 0.14 eV, and for Li{110}/*h*-BN, the differences are smaller than 0.10 eV. After adsorbed with a lithium atom at the interface, the *h*-BN can well preserve its structure and maintain a flat geometry, which can be validated by the analysis on the height variance of the atoms of *h*-BN after lithium adsorption as shown in Table 3. The small height variance reflects the high stiffness of *h*-BN, which can help preserve the structure of *h*-BN and suppress dendrite growth during the lithium plating process.

We then analyzed the relationship between the adsorption energy of lithium atoms at the interface and its relative position toward the lithium metal surface and *h*-BN. For each adsorption site at the interface, we added the lithium atom adsorption energies on the exact same site of bare lithium surface and *h*-BN, and compared the obtained results with the calculated interfacial adsorption energies as shown in Figure 7, where some data degenerated into one point. It is found that the adsorption energy of lithium atom at the interfaces can be estimated by the following equation:

$$E_{ads}(\text{interface}) = E_{ads}(\text{Li}_{surf}) + E_{ads}(h - \text{BN}_{surf}) + \delta, \quad \delta > 0 \tag{5}$$

where $E_{ads}(\text{Li}_{surf})$ is the adsorption energy of lithium on the lithium metal surface at the same adsorption site, $E_{ads}(h\text{-BN}_{surf})$ is the adsorption energy of lithium on *h*-BN at the same adsorption site, and δ is a small positive correction value. Thus, though only eight symmetrically different adsorption sites were considered in our calculations, the adsorption energy of lithium atom on other possible adsorption sites can be predicted, and our conclusion that the lithium adsorption energies at the interface are higher than those on bare lithium metal or *h*-BN is also expected to be valid for other possible adsorption sites. After the adsorption sites being fully occupied by lithium atoms, the newly adsorbed lithium atoms will become a new surface layer of lithium metal, and the space between the new lithium metal surface and *h*-BN can provide new adsorption sites.

Figure 8 plotted the charge transfer after lithium atom adsorbed at the interfaces on A1 and B1 sites, which provided the largest adsorption energies. In both cases, nitrogen atoms lose their electrons toward the undercover adsorbed lithium atom and the lithium metal surfaces. The strong charge transfer contributed to the enhanced adsorption energies, which help to

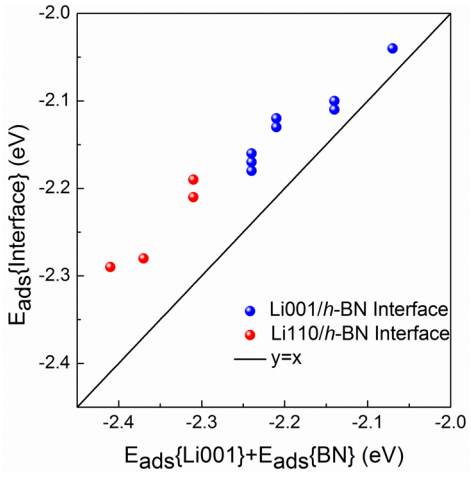

Figure 7. Correlation between the adsorption energy of lithium atom at Li/*h*-BN interfaces and the sum of its adsorption energies on bare lithium metal surface and *h*-BN at the same adsorption site.

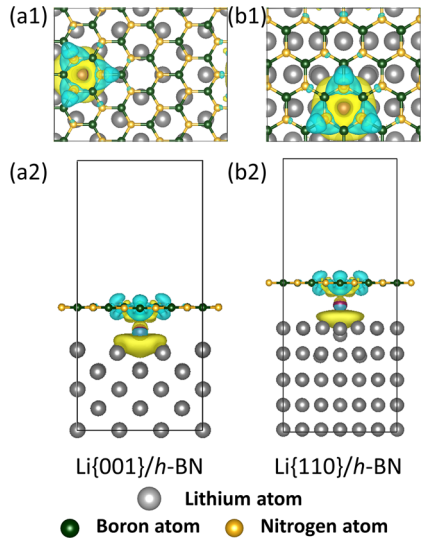

Figure 8. (a1),(b1) Top and (a2),(b2) side view of charge transfer after lithium atom adsorbed at the interfaces of Li/*h*-BN, where the blue area means charge deficient and the yellow area means charge sufficient. The iso-surface plotted is 0.001|e|/bohr^3.

DOI: 10.1021/acsami.6b14560
ACS Appl. Mater. Interfaces 2017, 9, 1987−1994

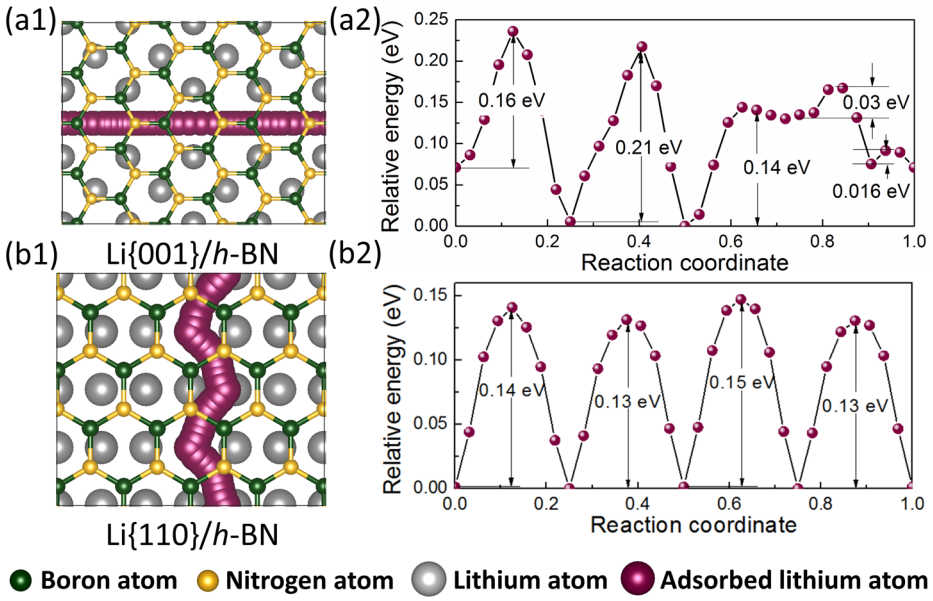

Figure 9. Lithium diffusion at the interfaces of (a1),(a2) Li{001}/*h*-BN and (b1),(b2) Li{110}/*h*-BN.

anchor the lithium atom at the interfaces instead of directly expose to the electrolyte, thus protecting the lithium from corrosion and maintaining the high Columbic efficiency. The high stiffness of *h*-BN can also effectively prevent the lithium atom from forming clusters which will induce strong structural deformation of *h*-BN, therefore suppressing lithium dendrite growth.

3.5. Lithium Ion Transport at the Li/*h*-BN Interfaces. In addition to the adsorption energy, the dendrite growth process is also affected by the metal ion diffusion capability at the metal surfaces, where the lower diffusion energy barrier could facilitate the even distribution of adsorbed metal atoms and mitigate the dendrite growth phenomenon.[44] We studied the lithium diffusion property of lithium atom at the interfaces via NEB method by putting images between the stable adsorption sites calculated in section 3.4 as shown in Figure 9a, and the corresponding diffusion energy barriers are plotted in Figure 9b. For the Li{001}/*h*-BN interface, the diffusion energy barriers are lower than 0.21 eV, and for the Li{110}/*h*-BN interface, the diffusion energy barriers are lower than 0.15 eV. These values are comparable with the sum of lithium migration energy barriers on pristine *h*-BN and corresponding lithium metal surfaces. The low lithium migration energy barriers together with the high stiffness of *h*-BN will synergistically promote the uniform distribution of lithium under the *h*-BN cover during the plating process and induce a layer-by-layer growth mechanism of the undercover lithium metal, eventually leading to a flat surface of the lithium metal anode.

4. CONCLUSIONS

In this article, we systematically studied the working mechanism of *h*-BN as the interfacial layer for lithium metal anode via first-principle calculations. It is found that the interaction between *h*-BN and lithium metal is a weak van der Waals force, and two atomic layers of *h*-BN can provide energy barriers large enough to prevent electron tunneling, which effectively prohibited the decomposition of electrolyte. The adsorption energies of lithium atom at the interfaces are much larger than those on pristine lithium metal surfaces or *h*-BN, ensuring that lithium metal will prefer to be deposited under the cover of *h*-BN, thus reducing the chance of direct contact between lithium metal and electrolyte and contributing to a high Columbic efficiency. The combined high stiffness of *h*-BN and low lithium migration energy barriers at the Li/*h*-BN interfaces can synergistically facilitate a uniform distribution of lithium under *h*-BN during the lithium plating process, therefore effectively suppressing lithium dendrite growth. Our research confirms that employing insulating 2D materials as the interfacial layer of lithium metal anode is a promising strategy to address the lithium dendrite problem, and further shed light on the design of lithium metal anode.

AUTHOR INFORMATION

Corresponding Author

*Tel.: (852) 2358 8647. E-mail: metzhao@ust.hk (T.Z.).

ORCID

Le Shi: 0000-0003-1468-4549

Ao Xu: 0000-0003-0648-2701

Tianshou Zhao: 0000-0003-4825-2381

Author Contributions

The manuscript was written through contributions of all authors. All authors have given approval to the final version of the manuscript.

Notes

The authors declare no competing financial interest.

ACKNOWLEDGMENTS

The work described in this paper was fully supported by a grant from the Research Grants Council of the Hong Kong Special Administrative Region, China (Project No. 16213414)

REFERENCES

(1) Etacheri, V.; Marom, R.; Elazari, R.; Salitra, G.; Aurbach, D. Challenges in the Development of Advanced Li-Ion Batteries: A Review. *Energy Environ. Sci.* **2011**, *4*, 3243−3262.

(2) Su, X.; Wu, Q.; Li, J.; Xiao, X.; Lott, A.; Lu, W.; Sheldon, B. W.; Wu, J. Silicon-Based Nanomaterials for Lithium-Ion Batteries: A Review. *Adv. Energy Mater.* **2014**, *4*, 1300882.

DOI: 10.1021/acsami.6b14560
ACS Appl. Mater. Interfaces 2017, 9, 1987−1994

(3) Nitta, N.; Wu, F.; Lee, J. T.; Yushin, G. Li-Ion Battery Materials: Present and Future. *Mater. Today* **2015**, *18*, 252−264.
(4) Jing, Y.; Zhou, Z.; Cabrera, C. R.; Chen, Z. Graphene, Inorganic Graphene Analogs and Their Composites for Lithium Ion Batteries. *J. Mater. Chem. A* **2014**, *2*, 12104−12122.
(5) Zhang, W. J. A Review of the Electrochemical Performance of Alloy Anodes for Lithium-Ion Batteries. *J. Power Sources* **2011**, *196*, 13−24.
(6) Ji, L.; Lin, Z.; Alcoutlabi, M.; Zhang, X. Recent Developments in Nanostructured Anode Materials for Rechargeable Lithium-Ion Batteries. *Energy Environ. Sci.* **2011**, *4*, 2682−2699.
(7) Goriparti, S.; Miele, E.; De Angelis, F.; Di Fabrizio, E.; Zaccaria, R. P.; Capiglia, C. Review on Recent Progress of Nanostructured Anode Materials for Li-Ion Batteries. *J. Power Sources* **2014**, *257*, 421−443.
(8) Aurbach, D.; Zinigrad, E.; Cohen, Y.; Teller, H. A Short Review of Failure Mechanisms of Lithium Metal and Lithiated Graphite Anodes in Liquid Electrolyte Solutions. *Solid State Ionics* **2002**, *148*, 405−416.
(9) Xu, W.; Wang, J.; Ding, F.; Chen, X.; Nasybulin, E.; Zhang, Y.; Zhang, J. G. Lithium Metal Anodes for Rechargeable Batteries. *Energy Environ. Sci.* **2014**, *7*, 513−537.
(10) Manthiram, A.; Fu, Y.; Su, Y. S. Challenges and Prospects of Lithium−Sulfur Batteries. *Acc. Chem. Res.* **2013**, *46*, 1125−1134.
(11) Manthiram, A.; Fu, Y.; Chung, S. H.; Zu, C.; Su, Y. S. Rechargeable Lithium−Sulfur Batteries. *Chem. Rev.* **2014**, *114*, 11751−11787.
(12) Girishkumar, G.; McCloskey, B.; Luntz, A. C.; Swanson, S.; Wilcke, W. Lithium-Air Battery: Promise and Challenges. *J. Phys. Chem. Lett.* **2010**, *1*, 2193−2203.
(13) Lu, Y. C.; Gallant, B. M.; Kwabi, D. G.; Harding, J. R.; Mitchell, R. R.; Whittingham, M. S.; Shao-Horn, Y. Lithium−Oxygen Batteries: Bridging Mechanistic Understanding and Battery Performance. *Energy Environ. Sci.* **2013**, *6*, 750−768.
(14) Li, Y.; Leung, K.; Qi, Y. Computational Exploration of the Li-Electrodel Electrolyte Interface in the Presence of a Nanometer Thick Solid-Electrolyte Interphase Layer. *Acc. Chem. Res.* **2016**, *49*, 2363−2370.
(15) Lin, Y. X.; Liu, Z.; Leung, K.; Chen, L. Q.; Lu, P.; Qi, Y. Connecting the Irreversible Capacity Loss in Li-Ion Batteries with the Electronic Insulating Properties of Solid Electrolyte Interphase (SEI) Components. *J. Power Sources* **2016**, *309*, 221−230.
(16) Liu, Z.; Qi, Y.; Lin, Y. X.; Chen, L.; Lu, P.; Chen, L. Q. Interfacial Study on Solid Electrolyte Interphase at Li Metal Anode: Implication for Li Dendrite Growth. *J. Electrochem. Soc.* **2016**, *163*, A592−A598.
(17) Shi, S.; Lu, P.; Liu, Z.; Qi, Y.; Hector, L. G., Jr; Li, H.; Harris, S. J. Direct Calculation of Li-Ion Transport in the Solid Electrolyte Interphase. *J. Am. Chem. Soc.* **2012**, *134*, 15476−15487.
(18) Liu, Y.; Lin, D.; Liang, Z.; Zhao, J.; Yan, K.; Cui, Y. Lithium-Coated Polymeric Matrix as a Minimum Volume-Change and Dendrite-Free Lithium Metal Anode. *Nat. Commun.* **2016**, *7*, 10992.
(19) Liang, Z.; Zheng, G.; Liu, C.; Liu, N.; Li, W.; Yan, K.; Yao, H.; Hsu, P. C.; Chu, S.; Cui, Y. Polymer Nanofiber-Guided Uniform Lithium Deposition for Battery Electrodes. *Nano Lett.* **2015**, *15*, 2910−2916.
(20) Mukherjee, R.; Thomas, A. V.; Datta, D.; Singh, E.; Li, J.; Eksik, O.; Shenoy, V. B.; Koratkar, N. Defect-Induced Plating of Lithium Metal within Porous Graphene Networks. *Nat. Commun.* **2014**, *5*, 3710.
(21) Ding, F.; Xu, W.; Graff, G. L.; Zhang, J.; Sushko, M. L.; Chen, X.; Shao, Y.; Engelhard, M. H.; Nie, Z.; Xiao, J.; Liu, X. Dendrite-Free Lithium Deposition via Self-Healing Electrostatic Shield Mechanism. *J. Am. Chem. Soc.* **2013**, *135*, 4450−4456.
(22) Li, W.; Yao, H.; Yan, K.; Zheng, G.; Liang, Z.; Chiang, Y. M.; Cui, Y. The Synergetic Effect of Lithium Polysulfide and Lithium Nitrate to Prevent Lithium Dendrite Growth. *Nat. Commun.* **2015**, *6*, 7436.
(23) Kim, J. S.; Kim, D. W.; Jung, H. T.; Choi, J. W. Controlled Lithium Dendrite Growth by a Synergistic Effect of Multilayered Graphene Coating and an Electrolyte Additive. *Chem. Mater.* **2015**, *27*, 2780−2787.
(24) Wu, F.; Qian, J.; Chen, R.; Lu, J.; Li, L.; Wu, H.; Chen, J.; Zhao, T.; Ye, Y.; Amine, K. An Effective Approach to Protect Lithium Anode and Improve Cycle Performance for Li−S Batteries. *ACS Appl. Mater. Interfaces* **2014**, *6*, 15542−15549.
(25) Mayers, M. Z.; Kaminski, J. W.; Miller, T. F., III Suppression of Dendrite Formation via Pulse Charging in Rechargeable Lithium Metal Batteries. *J. Phys. Chem. C* **2012**, *116*, 26214−26221.
(26) Aryanfar, A.; Brooks, D.; Merinov, B. V.; Goddard, W. A., III; Colussi, A. J.; Hoffmann, M. R. Dynamics of Lithium Dendrite Growth and Inhibition: Pulse Charging Experiments and Monte Carlo Calculations. *J. Phys. Chem. Lett.* **2014**, *5*, 1721−1726.
(27) Cheng, X. B.; Hou, T. Z.; Zhang, R.; Peng, H. J.; Zhao, C. Z.; Huang, J. Q.; Zhang, Q. Dendrite-Free Lithium Deposition Induced by Uniformly Distributed Lithium-Ions for Efficient Lithium Metal Batteries. *Adv. Mater.* **2016**, *28*, 2888−2895.
(28) Tung, S. O.; Ho, S.; Yang, M.; Zhang, R.; Kotov, N. A. A Dendrite-Suppressing Composite Ion Conductor from Aramid Nanofibres. *Nat. Commun.* **2015**, *6*, 6152.
(29) Kozen, A. C.; Lin, C. F.; Pearse, A. J.; Schroeder, M. A.; Han, X.; Hu, L.; Lee, S. B.; Rubloff, G. W.; Noked, M. Next-Generation Lithium Metal Anode Engineering via Atomic Layer Deposition. *ACS Nano* **2015**, *9*, 5884−5892.
(30) Li, N. W.; Yin, Y. X.; Yang, C. P.; Guo, Y. G. An Artificial Solid Electrolyte Interphase Layer for Stable Lithium Metal Anodes. *Adv. Mater.* **2016**, *28*, 1853−1858.
(31) Lepley, N. D.; Holzwarth, N. A. Modeling Interfaces between Solids: Application to Li Battery Materials. *Phys. Rev. B: Condens. Matter Mater. Phys.* **2015**, *92*, 214201.
(32) Lepley, N. D.; Holzwarth, N. A.; Du, Y. A. Structures, Li^+ Mobilities, and Interfacial Properties of Solid Electrolytes Li_3PS_4 and Li_3PO_4 from First Principles. *Phys. Rev. B: Condens. Matter Mater. Phys.* **2013**, *88*, 104103.
(33) Hao, S.; Wolverton, C. Lithium Transport in Amorphous Al_2O_3 and AlF_3 for Discovery of Battery Coatings. *J. Phys. Chem. C* **2013**, *117*, 8009−8013.
(34) Jung, S. C.; Han, Y. K. How Do Li Atoms Pass through the Al_2O_3 Coating Layer during Lithiation in Li-ion Batteries? *J. Phys. Chem. Lett.* **2013**, *4*, 2681−2685.
(35) Santosh, K. C.; Longo, R. C.; Xiong, K.; Cho, K. Electrode-Electrolyte Interface for Solid State Li-Ion Batteries: Point Defects and Mechanical Strain. *J. Electrochem. Soc.* **2014**, *161*, F3104−F3110.
(36) Yan, K.; Lee, H. W.; Gao, T.; Zheng, G.; Yao, H.; Wang, H.; Lu, Z.; Zhou, Y.; Liang, Z.; Liu, Z.; Chu, S. Ultrathin Two-Dimensional Atomic Crystals as Stable Interfacial Layer for Improvement of Lithium Metal Anode. *Nano Lett.* **2014**, *14*, 6016−6022.
(37) Giannozzi, P.; Baroni, S.; Bonini, N.; Calandra, M.; Car, R.; Cavazzoni, C.; Ceresoli, D.; Chiarotti, G. L.; Cococcioni, M.; Dabo, I.; Dal Corso, A. QUANTUM ESPRESSO: A Modular and Open-Source Software Project for Quantum Simulations of Materials. *J. Phys.: Condens. Matter* **2009**, *21*, 395502.
(38) Perdew, J. P.; Ernzerhof, M.; Burke, K. Rationale for Mixing Exact Exchange with Density Functional Approximations. *J. Chem. Phys.* **1996**, *105*, 9982−9985.
(39) Blöchl, P. E. Projector Augmented-Wave Method. *Phys. Rev. B: Condens. Matter Mater. Phys.* **1994**, *50*, 17953.
(40) Grimme, S. Semiempirical GGA-Type Density Functional Constructed with a Long-Range Dispersion Correction. *J. Comput. Chem.* **2006**, *27*, 1787−1799.
(41) Jing, Y.; Zhou, Z.; Cabrera, C. R.; Chen, Z. Metallic VS_2 Monolayer: A Promising 2D Anode Material for Lithium Ion Batteries. *J. Phys. Chem. C* **2013**, *117*, 25409−25413.
(42) Jónsson, H.; Mills, G.; Jacobsen, K. W. In *Classical and Quantum Dynamics in Condensed Phase Simulations*; Berne, B. J., Ciccotti, G., Coker, D. F., Eds.; World Scientific: Singapore, 1998; p 385.

DOI: 10.1021/acsami.6b14560
ACS Appl. Mater. Interfaces 2017, 9, 1987−1994

(43) Anderson, M. S.; Swenson, C. A. Experimental Equations of State for Cesium and Lithium Metals to 20 kbar and the High-Pressure Behavior of the Alkali Metals. *Phys. Rev. B: Condens. Matter Mater. Phys.* **1985**, *31*, 668.
(44) Jäckle, M.; Groß, A. Microscopic Properties of Lithium, Sodium, and Magnesium Battery Anode Materials Related to Possible Dendrite Growth. *J. Chem. Phys.* **2014**, *141*, 174710.
(45) Jin, C.; Lin, F.; Suenaga, K.; Iijima, S. Fabrication of a Freestanding Boron Nitride Single Layer and Its Defect Assignments. *Phys. Rev. Lett.* **2009**, *102*, 195505.

DOI: 10.1021/acsami.6b14560
ACS Appl. Mater. Interfaces 2017, 9, 1987−1994